Green Energy and Intelligent Transportation 5 (2026) 100307

Contents lists available at ScienceDirect

Green Energy and Intelligent Transportation

journal homepage: www.journals.elsevier.com/green-energy-and-intelligent-transportation

Full length article

Design and implementation of interoperable high-efficiency bidirectional wireless power transfer systems for multiple vehicles

Baokun Zhang [a], Junjun Deng [a,*], Mengchen Duan [a], Chang Li [a], Yi Zheng [a], Shuo Wang [a], David Dorrell [b]

[a] National Engineering Research Center of Electric Vehicles, Beijing Institute of Technology, Beijing 100081, China
[b] Department of Mechanical and Material Engineering, University of Turku, Turku 20014, Finland

HIGHLIGHTS

- Bidirectional EV wireless interfaces enable power flow in both directions.
- Modular design ensures high efficiency under wide operating conditions.
- A ground assembly supports interoperability with three vehicle assemblies.

GRAPHICAL ABSTRACT

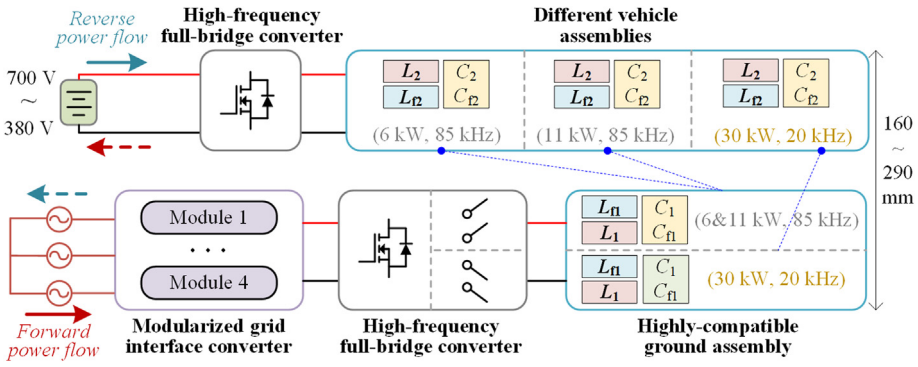

ARTICLE INFO

Keywords:
Bidirectional
Compatibility
Efficiency
Interoperability
Wireless power transfer

ABSTRACT

The rapid growth of electric vehicle ownership and advancements in vehicle-to-grid (V2G) technologies have created an urgent demand for bidirectional charging–discharging interfaces. Wireless power transfer (WPT) technology, known for its convenience, safety, and flexibility, is a promising solution for energy transfer between vehicles and the grid. This paper presents the design and demonstration of a highly interoperable and high-efficiency bidirectional WPT system, addressing key challenges such as wide voltage output adaptation, multi-power level compatibility, and efficient operation over a broad power range. The front-end converter uses a power module combining a three-phase fully controlled rectifier and a cascaded buck converter to provide a wide DC voltage range. Modular activation technology ensures the grid interface operates efficiently under varying power demands. For the bidirectional inductive power transfer (BIPT) link, an integrated scheme for the resonant networks in the ground assembly (GA) with cross-frequency compatibility is proposed, and its performance is validated through calculations and simulations. A bidirectional power flow control strategy is implemented, with voltage regulation and operation mode switching as the main method. Experimental results demonstrate interoperability between the same grid-side equipment and different vehicle-side equipment rated at 6, 11, and 30 kW. Under specified operating conditions at the aligned position, the system achieves a grid-to-battery efficiency from 91.7% to 94.3%, and a battery-to-grid efficiency ranging from 89.5% to 93.5%.

* Corresponding author. Beijing Institute of Technology, No.5 Zhongguancun South Street, Haidian District, Beijing, China.
E-mail address: dengjunjun@bit.edu.cn (J. Deng).

https://doi.org/10.1016/j.geits.2025.100307
Received 30 December 2024; Received in revised form 14 February 2025; Accepted 5 March 2025
Available online 28 March 2025

1. Introduction

With the global focus on clean energy and sustainable development, electric vehicle (EV) ownership has experienced rapid growth over the past decade. According to the International Energy Agency (IEA), global EV ownership exceeded 40 million at the end of 2023 [1]. This trend suggests technological advancements, supportive policies, and heightened public environmental awareness.

However, the large-scale adoption of EVs presents challenges such as grid load management, particularly during peak-hour charging. Vehicle-to-Grid (V2G) technology offers a promising solution by enable energy flow between EVs and the grid. This technology allows EVs to act as mobile energy storage units, feeding stored electricity back into the grid during peak demand and drawing power during off-peak hours. This dynamic interaction helps balance grid loads, improve energy utilization, and integrate renewable energy sources more effectively.

In recent years, bidirectional wireless power transfer (BWPT) systems have gained increasing attention as an attractive interface. Leveraging the principle of electromagnetic induction, these systems enable contactless power transmission. Unlike traditional conductive charging methods, BWPT technology eliminates manual plugging and unplugging, offering a seamless and intelligent mechanism for automatic power exchange between the grid and EVs.

A typical two-stage BWPT system consists of a grid interface converter and a bidirectional inductive power transfer (BIPT) link. The literature on bidirectional EV wireless charging and discharging highlights the ability of BIPT links to control bidirectional power flow, and diverse compensation topologies, coil types, and control strategies have been developed and applied [2–7]. However, research has largely focused on the BIPT link itself, with limited attention given to the overall performance on the bidirectional charge–discharge interface [8–10]. The primary technical challenge lies in achieving joint control of multi-stage power conversion and multiple control variables to ensure flexible power flow adjustment and high efficiency over a wide operating range.

The prototypes developed in these studies are often tailored to specific power levels or vehicle models. However, a BWPT system that can accommodate various vehicle models with a wide voltage range and multiple power levels is still lacking. The main technical challenge lies in ensuring interoperability between the ground assembly (GA) and various vehicle assemblies (VAs), particularly in transferring the target power between devices with differing voltage, power, air gap, and other parameters.

The interoperability of wireless charging systems refers to the capability of different transmitter and receiver devices to realize information interaction and satisfy performance and functional requirements [11], primarily categorized into communication, magnetic, and electrical interoperability [12]. In this work, the system performance of the GA and various VAs under different gaps and voltage levels serve as the key criteria for evaluating interoperability, particularly in terms of output power and efficiency.

The purpose of this work is to develop wireless bidirectional charging and discharging equipment that is adaptable to multiple vehicle types, and realize efficient transmission and conversion of electric energy over a wide operating range. Specifically, the proposed BWPT system offers the following key features:

1) A modular adaptive switching grid interface converter that adjusts the number of active modules based on the required output, enabling efficient operation across a wide voltage and power range;
2) The GA integrates two sets of resonant networks operating at different frequencies, providing compatibility with multiple VAs at various power levels by enabling each set independently;
3) A modulation and control strategy, incorporating multiple variables and operation modes, enables flexible control over power flow direction and magnitude, ensuring high-efficiency power transmission and conversion.

Table 1
Specifications of the three target vehicles.

Vehicle No.	1	2	3
Power level/kW	6	11	30
Battery voltage range/V	380–440	600–700	420–610
Nominal battery voltage/V	400	660	550
Ground clearance range/mm	190–210	160–180	270–290
Operating frequency/kHz	85	85	20

The paper is organized as follows: Section 2 outlines the requirements of this study and presents the design of each key component; in Section 3, the operation mode and control methods for the system are analysed, which consists of multiple power conversion stages; Section 4 showcases the prototype of the developed system and the experimental results under various test conditions; and finally, Section 5 concludes the work.

2. System design

This section begins with an analysis of the requirements and main challenges of the target vehicle models. Using the concept of task decoupling, the design considerations for the grid interface converter, compensation circuit, and magnetic coupler are presented successively.

2.1. Requirements analysis for different vehicles

Three target vehicles were selected with different battery voltage ranges, ground clearance, and power requirements, as summarized in Table 1. $U_{\text{out-min}}$, $U_{\text{out-nom}}$, and $U_{\text{out-max}}$ denote the minimum voltage, rated voltage, and maximum voltage of the vehicle power battery, respectively. The system is designed to achieve full power output using the rated voltage. For ground clearance, the distance between the chassis and the ground at the VA installation site is considered, taking into account factors such as tire pressure and other potential influences.

According to the technical requirements for wireless charging (power transmission) equipment issued by the Ministry of Industry and Information Technology of China, the operating frequency for wireless charging equipment for electric vehicles with a rated transmission power between 22 and 120 kW is 19–21 kHz, while equipment with a rated transmission power of 22 kW or less operates at 79–90 kHz. Therefore, a central frequency of 85 kHz is selected for 6 and 11 kW equipment, and 20 kHz is selected for 30 kW equipment. Consequently, the power level and operating frequency for each VA are determined. For the GA, if a single resonant network is required to operate across two widely separated frequency bands, it would necessitate structural or parameter adjustments to the compensation network, significantly increasing design

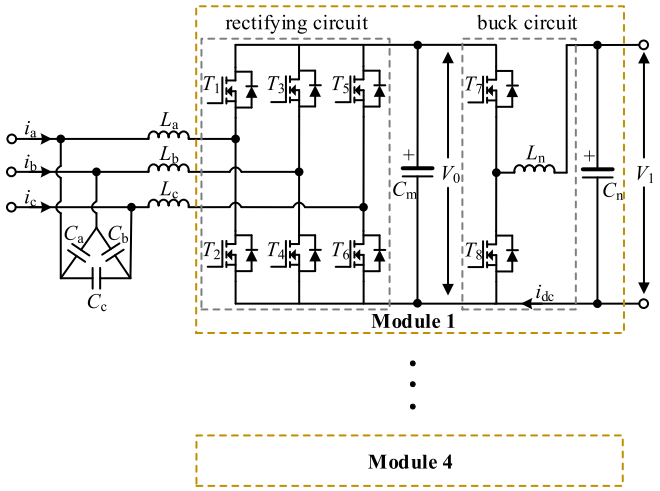

Fig. 1. Topology of the grid interface converter.

and control complexity. To address this, two separate resonant networks with distinct operating frequencies, each independently enabled, can be integrated to meet the VA's charging and discharging requirements. The difficulty lies in the integration and driving mechanism of these resonant networks.

2.2. Grid interface power converters

This section focuses on the grid interface converters. In a BWPT system, the AC-DC converter on the grid side typically requires a power factor correction (PFC) function to improve power factor and reduce current harmonic distortion. During forward operation, it converts the grid power-frequency AC into DC. Conversely, in reverse operation, it converts the DC from the BIPT link into AC and returns it to the grid.

In this work, the grid-side interface converter topology is shown in Fig. 1. It consists of a rectifier circuit, a buck circuit, and filtering components C_a, C_b, C_c, L_a, L_b, L_c, C_m, C_n, and L_n. For forward power flow, the three-phase AC input from the grid is transmitted to the rectifier circuit through the filtering network composed of C_a, C_b, C_c, L_a, L_b, and L_c. The rectifier circuit uses a three-phase six-switch topology, consisting of three bridge arms, with each bridge arm made up of two power switches with complementary switching states (e.g., T_1 and T_2 form one bridge arm). A sinewave pulse width modulation (SPWM) technique is used to make the input current follow the input voltage, ensuring the input current remains sinusoidal, achieving power factor correction, and providing a stable DC output voltage V_0.

By controlling the combination of the on-off states of the switching devices in the three bridge arms, the output voltage can be effectively regulated. This enables the three-phase active rectifier to exhibit a boost voltage characteristic and achieve output voltages exceeding 538 V (i.e., the peak line-to-line voltage of a 380 V grid). If the output voltage V_0 is directly used as the input to the BIPT link, although adjusting control variables such as phase shift angles and frequency can modify the output voltage, this method may reduce efficiency, or become infeasible under extreme voltage conditions. To enhance flexibility as well as accommodate a wide output voltage range of 380–700 V, additional power conversion stages are required. Therefore, a buck circuit is added after the rectifier circuit to step down the rectified output voltage V_0 to the DC-link voltage V_1. It consists of power switches T_7 and T_8, an output filter inductor L_n, and a DC bus capacitor C_n. The output voltage is adjusted by controlling the duty cycle of power switch T_7.

Achieving efficient operation over a wide power range is another challenge, as most power converters suffer from low efficiency at light loads. To address this issue, this work uses the concept of module adaptive switching technology. The front-end converter is designed in parallel with four low-power modules. Depending on the output power level, the appropriate number of modules is activated, ensuring that the operating modules remain within their high-efficiency operating range.

2.3. Compensation topology

SS and LCC–LCC are the most commonly used compensation topologies in existing BWPT systems. The choice of topology depends on two main factors. The first is the feasibility of achieving the desired inductances. Once the voltage, frequency, and power level are determined, the required self-inductance or mutual inductance can be estimated. For instance, if SS topology is used for the 30 kW system, the required mutual inductance is approximately 65 μH, and the self-inductance would likely exceed 300 μH. Given the size constraints of the VA, achieving this is challenging, and SS topology is therefore abandoned.

The second factor depends on the topology characteristics and application scenarios. The SS topology is simple, with few passive components, resulting in lower conduction losses in resonant networks. Systems based on SS topology offer high efficiency in applications with enough magnetic couplings and low misalignment tolerance requirements [13]. However, for EV wireless charging, which typically involves varying airgaps and misalignments leading to decrease in the coupling coefficient, the efficiency is significantly reduced and additional precautions are necessary to avoid overcurrent risks [14]. In contrast, LCC topology is less sensitive to changes in the coupling coefficient and load variations on both the primary and secondary sides [9]. Furthermore, as the coupling coefficient decreases, the current in the coils also decreases, eliminating the need for additional current-limiting measures. Therefore, the LCC–LCC compensation configuration is more suitable for EV wireless charging.

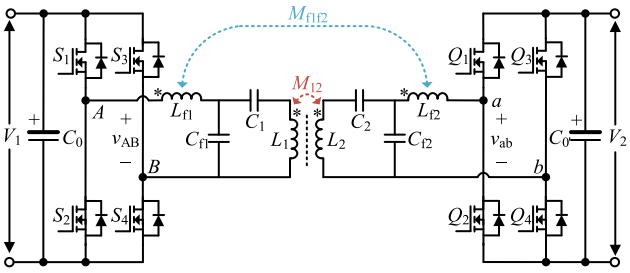

Fig. 2. Dual-coupled LCC–LCC topology-based BIPT system.

Compared to the traditional single-coupled LCC–LCC topology, the dual-coupled LCC–LCC topology may be a better choice, featuring additional power transmission paths in addition to the main coils. The magnetic couplings of compensation inductors help improve output performance under misaligned conditions [15,16]. Therefore, the dual-coupled LCC–LCC topology is finally selected as the compensation topology, and the BIPT link is shown in Fig. 2. V_1 and V_2 represent the dc-link voltage and battery voltage, respectively. C_0 and C_0 are the dc-link capacitors. S_1~S_4, and Q_1~Q_4 are the power MOSFETs of the full bridge (FB) converters on the grid side and vehicle side, respectively. C_1, C_2, C_{f1}, and C_{f2} are compensation capacitors. L_1 and L_2 are the main coils, while L_{f1} and L_{f2} are the compensation inductors. M_{12} and M_{f1f2} are the mutual inductance of the main coils and the compensation inductors, respectively. v_{AB} and v_{ab} are the output voltages of the full bridge converters.

The topology parameters are designed by the following equations to achieve a constant resonant angular frequency ω

$$\begin{aligned} &L_{f1}C_{f1} = 1/\omega^2,\ L_{f2}C_{f2} = 1/\omega^2 \\ &(L_1 - L_{f1})C_1 = 1/\omega^2,\ (L_2 - L_{f2})C_2 = 1/\omega^2 \end{aligned} \tag{1}$$

The equivalent circuit of the resonant network is presented in Fig. 3. Using fundamental harmonics approximation (FHA) for analysis, U_{AB} and U_{ab} represent the RMS values of the fundamental components of the excitation voltages. $\dot{I}_{f1}$, $\dot{I}_1$, $\dot{I}_2$, $\dot{I}_{f2}$ represent the current flowing through the coils. R_{f1}, R_{p1}, R_{p2}, R_{f2} are the equivalent series resistance (ESR) of each branch.

By applying the Kirchhoff Voltage Law, the current through the compensation inductors and main coils can be given as

$$\begin{aligned} &\dot{I}_{f1} = \frac{jM_{12}\dot{U}_{ab}}{\omega\left(L_{f1}L_{f2} + M_{12}M_{f1f2}\right)},\ \dot{I}_{f2} = \frac{jM_{12}\dot{U}_{AB}}{\omega\left(L_{f1}L_{f2} + M_{12}M_{f1f2}\right)} \\ &\dot{I}_1 = -\frac{jL_{f2}\dot{U}_{AB}}{\omega\left(L_{f1}L_{f2} + M_{12}M_{f1f2}\right)},\ \dot{I}_2 = -\frac{jL_{f1}\dot{U}_{ab}}{\omega\left(L_{f1}L_{f2} + M_{12}M_{f1f2}\right)} \end{aligned} \tag{2}$$

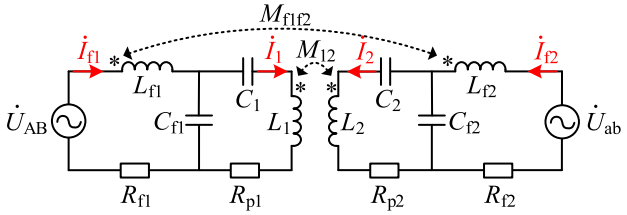

Fig. 3. Equivalent circuit of the resonant network.

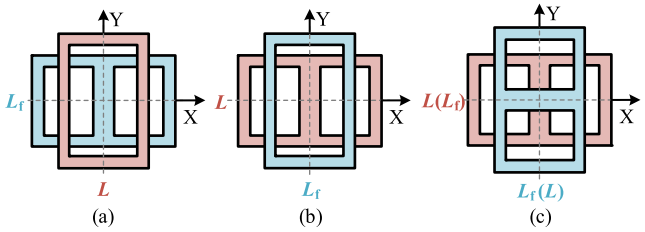

Fig. 4. Three integrated coil schemes.

Once the voltage combination and power level are determined, the desired I_{f1} and I_{f2} are limited to within a narrow range and should be achieved by adjusting the four inductances (L_{f1}, L_{f2}, M_{12}, and M_{f1f2}). The values of I_1 and I_2 then depend on the ratio of the compensation inductance L_{f1} (L_{f2}) to the main mutual inductance M_{12}.

Similarly, the voltage stress across the coils and capacitors are also related to the four inductances, and they are expressed as

$$\begin{aligned} U_{Lf1} &= \frac{L_{f1}M_{12}U_{ab}}{L_{f1}L_{f2}+M_{12}M_{f1f2}},\ U_{Lf2} = \frac{L_{f2}M_{12}U_{AB}}{L_{f1}L_{f2}+M_{12}M_{f1f2}} \\ U_{L1} &= \frac{L_{f2}L_1U_{AB}}{L_{f1}L_{f2}+M_{12}M_{f1f2}},\ U_{L2} = \frac{L_{f1}L_2U_{ab}}{L_{f1}L_{f2}+M_{12}M_{f1f2}} \end{aligned} \tag{3}$$

$$\begin{aligned} U_{Cf1} &= \frac{L_{f1}\sqrt{M_{12}^2U_{ab}^2+L_{f2}^2U_{AB}^2}}{L_{f1}L_{f2}+M_{12}M_{f1f2}},\ U_{Cf2} = \frac{L_{f2}\sqrt{M_{12}^2U_{AB}^2+L_{f1}^2U_{ab}^2}}{L_{f1}L_{f2}+M_{12}M_{f1f2}} \\ U_{C1} &= \frac{(L_1-L_{f1})L_{f2}U_{AB}}{L_{f1}L_{f2}+M_{12}M_{f1f2}},\ U_{C2} = \frac{(L_2-L_{f2})L_{f1}U_{ab}}{L_{f1}L_{f2}+M_{12}M_{f1f2}} \end{aligned} \tag{4}$$

2.4. Magnetic couplers

For practical applications, integrating both the compensation inductor and the main coil within the GA or VA is preferable to enable miniaturization. According to the magnetic flux distribution patterns of unipolar and bipolar coils, several integrated coil schemes have been proposed [17–19]. These schemes can effectively minimize same-side cross-coupling when arranged as shown in Fig. 4. Notably, DD coils offer approximately 1.7 times higher inductance per turn compared to similar rectangular coils [20]. Under specific self-inductance requirements, using DD coils can reduce the external dimensions or the number of turns, thereby meeting compact design requirements and reducing material consumption. Consequently, the integrated coil scheme (c) is adopted.

The internal layout of magnetic couplers is illustrated in Fig. 5. The coils are mounted on 1 mm thick plastic coil formers, stacked sequentially. The 30 kW coils are placed in direct contact with ferrite cores within the GA for a shorter heat conduction path. Heat is transferred to the aluminum backplate via potting adhesive and dissipated by the heat sink fins. For the VAs, the cooling methods include liquid cooling for the 11 and 30 kW equipment, and natural cooling for the 6 kW equipment.

The Mn–Zn Ferrite cores of a DMR95, specifically model EI 40(I), were selected for their high permeability and low core loss characteristics. The resonant capacitor is formed from CELEM conduction-cooled capacitors, which are well-suited for high-power applications. The selection process follows these principles: first, prioritize existing specifications; second, minimize the number of capacitors used, if the required voltage rating exceeds the capacity of a single capacitor, multiple capacitors of the same model are connected in series to handle higher voltage stress; and third, ensure a safe margin of at least 10% for both voltage and current limits.

To minimize skin-effect loss, AWG 38 wire with a strand diameter of 0.1 mm was selected. The Litz wire has a voltage limit of 3,000 V_{rms}, and a current density of 4 A/mm^2 is used to calculate the required number of strands. In addition to the electrical constraints outlined above, there are mechanical constraints, primarily concerning the maximum size of the magnetic couplers. Since the GA generally has more available space compared to the limited area under the vehicle chassis, and to ensure that the VA remains compact and lightweight, an asymmetric parameter design is used, with $L_1 > L_2$. The values of L_{f1} and L_{f2} can be set equal to simplify the design and reduce variable complexity. Once the outer dimensions and airgaps of the coils are determined, the coupling coefficients k_{12} and k_{f1f2} can be estimated using finite element analysis (FEA) simulations. Based on the available chassis space of the three vehicles, the external dimensions of the VA are set to 590 mm × 448 mm, 576 mm × 460 mm, and 800 mm × 610 mm, respectively, while the GA external dimensions are fixed at 1,064 mm × 910 mm.

Fig. 6 presents the parameter design procedure used in this study. The process starts with determining C_f and L_f. Subsequently, the required ranges for mutual inductance M_{12} and M_{f1f2} are estimated, allowing for a set of L and C values to be derived using the coupling coefficients obtained from finite element simulations. It is then assessed as to whether the desired inductance can be realized within dimensional constraints, and if the required capacitance can be obtained through a series connection. If feasible, the structural parameters of each winding are designed to achieve the target inductance values. The number of strands is determined first; second, the dimensions of the coil and magnetic cores are designed to ensure the coupling coefficient k approaches the target value; third, the number of turns and turn spacing are incrementally adjusted to verify whether the self-inductance and mutual inductance meet the requirements. The current and voltage stresses are rhencalculated to ensure they remain within allowable limits. If any condition is not met, the process reverts to the parameter selection stage, repeating the steps until all criteria are fulfilled.

The placement of the two GA coil sets presents another design consideration. Fig. 7 illustrates two integration schemes, both incorporating the 30 kW coils arranged as shown in Fig. 5(c). In the first scheme, the low-power coils also follow Fig. 5(c), while in the second scheme, the low-power coils are rotated by 90°.

As shown in Fig. 8(a), when the GA uses the first integration scheme, the 20 kHz resonant network is activated for pairing with the 30 kW VA. Simultaneously, the 85 kHz resonant network branch of L_{f1} is open, while L_1, C_1, and C_{f1} form a closed loop. This configuration requires consideration of the same-side cross-coupling $M_{11'}$ and different-side cross-coupling $M_{1'2}$. Similarly, Figs. 8(b)–(d) illustrate the mutual inductance models for the first scheme with the low-power VA, as well as the second

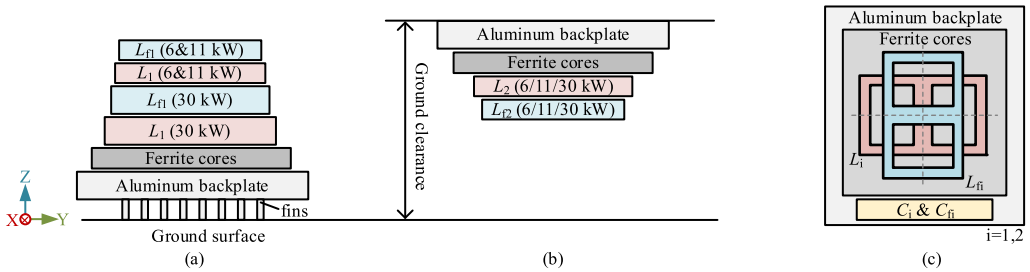

Fig. 5. Layout of internal components: front views of (a) GA, (b) VA, (c) top views.

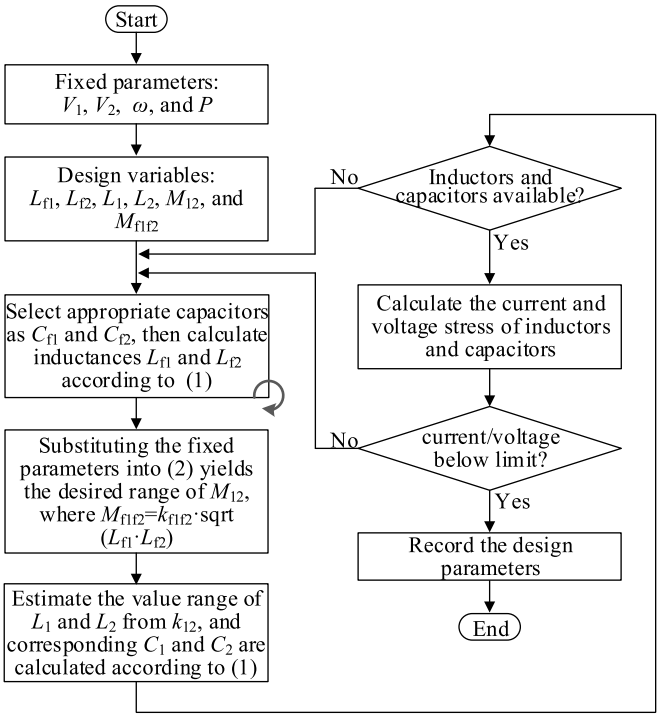

Fig. 6. Design procedure of key parameters.

scheme with the 30 kW and low-power VAs, respectively. The first integration scheme causes significant deviations in the self-inductance of the main coil from its design value due to the influence of the additional closed loop in another resonant network. This scheme is therefore discarded. In contrast, the second scheme has minimal impact on the coil self-inductance and is selected for further analysis.

The FHA analysis in section 2.3 provides approximate formulas, and it is useful for obtaining preliminary design parameters in the early stages. Even so, when the additional closed loop and all cross-couplings are considered, FHA is not no longer applicable. This is because the circuit contains multiple closed loops with different resonant frequencies, making it not suitable to consider only the fundamental harmonic component. The large number of cross-couplings complicates analytical expressions and makes them difficult to apply. Therefore, this study uses a numerical method to solve the specific time-domain model.

The resonant network when GA adopts the second integration scheme to match 30 kW VA (Fig. 8(c)) is analyzed as an example. The equivalent circuit is redrawn as shown in Fig. 9. Among the parameters, L_e, C_{1e} and C_{f1e} are the inductor and capacitors of the 85 kHz closed loop, while the others belong to the 20 kHz resonant networks, and $C_e = C_{1\text{-}e}\cdot C_{f1\text{-}e}/(C_{1\text{-}e} + C_{f1\text{-}e})$. The mutual inductance parameters of this circuit include the main mutual inductances: M_{12} and M_{f1f2}, the cross-couplings due to the closed loop: $M_{1'f1}$and $M_{1'f2}$, and the cross-couplings at misaligned position: M_{1f2}, M_{2f1}, and $M_{1'2}$. It should be noted that due to the decoupled arrangement of the coils, the mutual inductances M_{1f1}, M_{2f2}, and $M_{11'}$ are always zero and therefore ignored in the circuit.

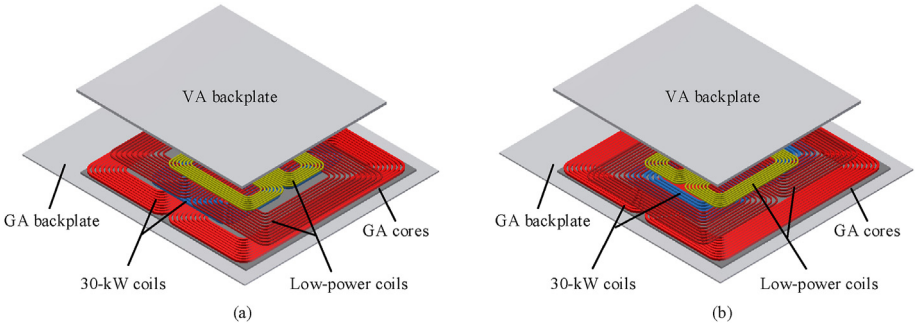

Fig. 7. Finite element model of VA and GA with two integration schemes of low-power coils.

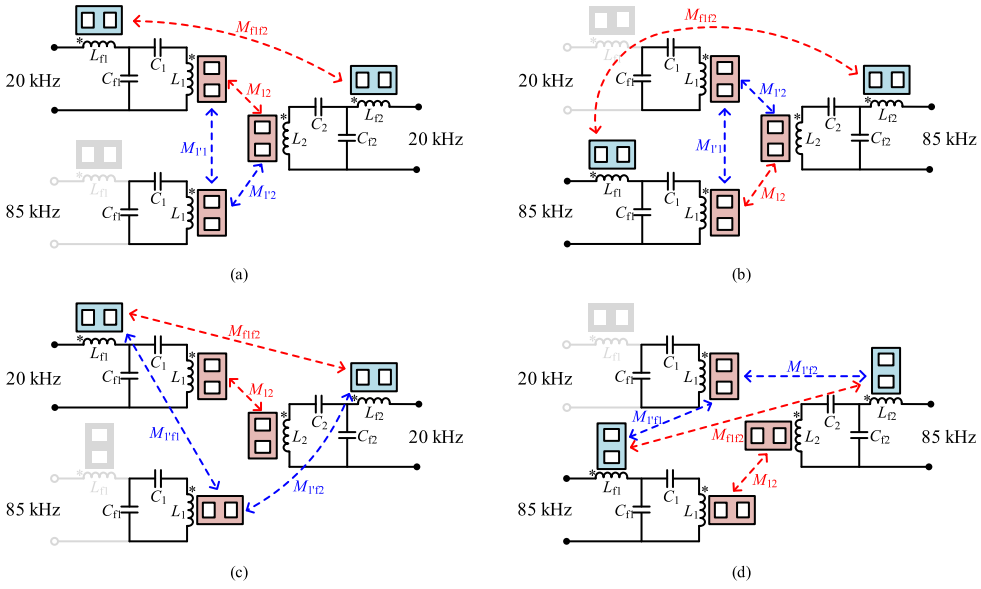

Fig. 8. GA using the first integration scheme with (a) 30 kW VA, (b) low-power VAs and GA using the second integration scheme with (c) 30-kW VA, (d) low-power VAs.

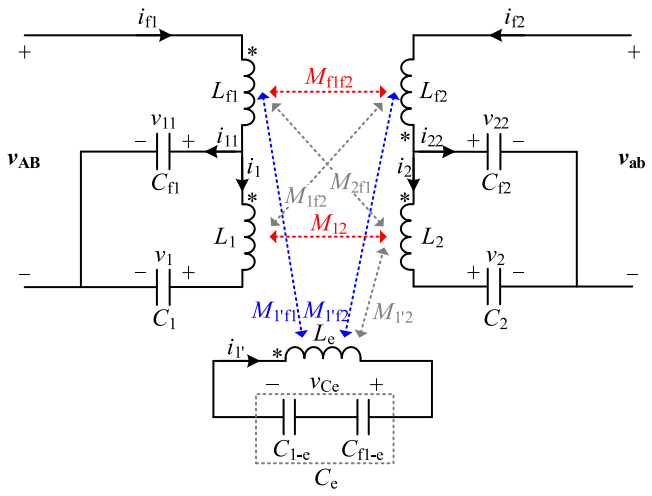

Fig. 9. Circuit model of the dual-coupled LCC–LCC topology considering all mutual inductances.

The solving method follows the method outlined in Ref. [21], which presents state-space time-domain models for conventional compensation topologies such as SS and single-coupled LCC–LCC. Building on this, this work extends the analysis to the dual-coupled LCC–LCC topology, incorporating the closed-loop and all cross-couplings.

Applying Kirchhoff Voltage Law, the following equation is obtained

$$\begin{cases} v_{11} = L_1\dfrac{di_1}{dt} + M_{12}\dfrac{di_2}{dt} - M_{1f2}\left(\dfrac{di_2}{dt} + \dfrac{di_{22}}{dt}\right) + v_1 \\ v_{22} = L_2\dfrac{di_2}{dt} + M_{12}\dfrac{di_1}{dt} + M_{2f1}\left(\dfrac{di_1}{dt} + \dfrac{di_{11}}{dt}\right) + M_{1'2}\dfrac{di_{1'}}{dt} + v_2 \\ v_{AB} = L_{f1}\left(\dfrac{di_1}{dt} + \dfrac{di_{11}}{dt}\right) - M_{f1f2}\left(\dfrac{di_2}{dt} + \dfrac{di_{22}}{dt}\right) + M_{2f1}\dfrac{di_2}{dt} + M_{1'f1}\dfrac{di_{1'}}{dt} + v_{11} \\ v_{ab} = L_{f2}\left(\dfrac{di_2}{dt} + \dfrac{di_{22}}{dt}\right) - M_{f1f2}\left(\dfrac{di_1}{dt} + \dfrac{di_{11}}{dt}\right) - M_{1f2}\dfrac{di_1}{dt} + M_{1'f2}\dfrac{di_{1'}}{dt} + v_{22} \\ 0 = L_e\dfrac{di_{1'}}{dt} + M_{1'f1}\left(\dfrac{di_1}{dt} + \dfrac{di_{11}}{dt}\right) + M_{1'f2}\left(\dfrac{di_2}{dt} + \dfrac{di_{22}}{dt}\right) + M_{1'2}\dfrac{di_2}{dt} + v_{Ce} \end{cases} \tag{5}$$

The capacitor voltages are $\boldsymbol{v} = [v_1(t), v_2(t), v_{11}(t), v_{22}(t), v_{Ce}(t)]$, capacitor currents are $\boldsymbol{i} = [i_1(t), i_2(t), i_{11}(t), i_{22}(t), i_{1'}(t)]$, and input voltage of the resonant tanks are $\boldsymbol{u} = [v_{AB}(t), v_{ab}(t)]$. The mathematical model can be rewritten in matrix format

$$\begin{cases} \boldsymbol{LC}\ddot{\boldsymbol{v}} + \boldsymbol{v} = \boldsymbol{Ku} \\ \boldsymbol{i} = \boldsymbol{C}\dot{\boldsymbol{v}} \end{cases} \tag{6}$$

where $\boldsymbol{L}$, $\boldsymbol{C}$, and $\boldsymbol{K}$ are the inductance matrix, capacitance matrix, and voltage-modified matrix, which are defined as

$$\boldsymbol{L} = \begin{bmatrix} L_1 + L_{f1} & M_{12} - M_{f1f2} + M_{2f1} - M_{1f2} & L_{f1} & -M_{f1f2} - M_{1f2} & M_{1'f1} \\ M_{12} - M_{f1f2} - M_{1f2} + M_{2f1} & L_2 + L_{f2} & -M_{f1f2} + M_{2f1} & L_{f2} & M_{1'f2} + M_{1'2} \\ L_{f1} & -M_{f1f2} + M_{2f1} & L_{f1} & -M_{f1f2} & M_{1'f1} \\ -M_{f1f2} - M_{1f2} & L_{f2} & -M_{f1f2} & L_{f2} & M_{1'f2} \\ M_{1'f1} & M_{1'f2} + M_{1'2} & M_{1'f1} & M_{1'f2} & L_e \end{bmatrix} \tag{7}$$

$$\boldsymbol{C} = \begin{bmatrix} C_1 & & & & \\ & C_2 & & & \\ & & C_{f1} & & \\ & & & C_{f2} & \\ & & & & C_e \end{bmatrix} \tag{8}$$

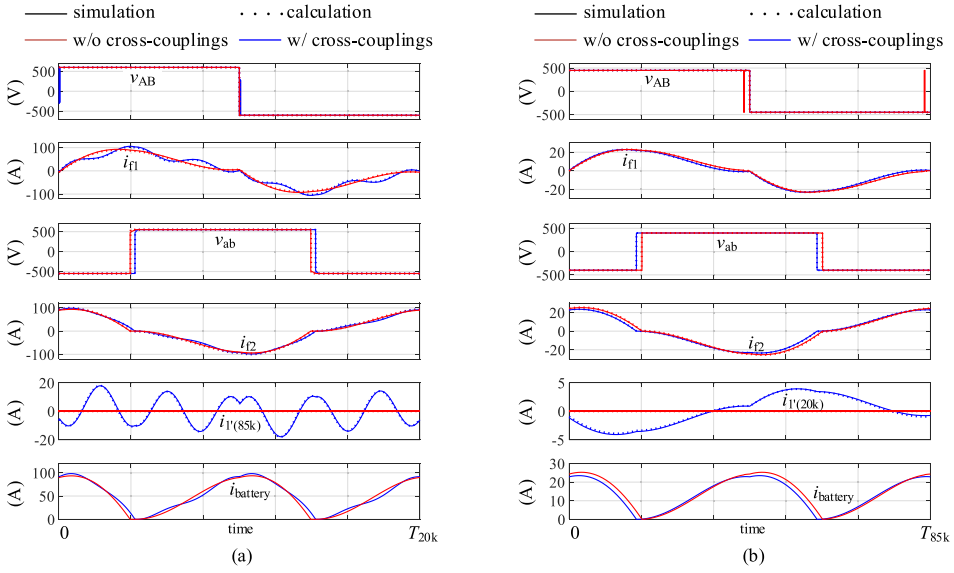

Fig. 10. Waveforms using the second integrated scheme, (a) 30-kW pair, (b) 6-kW pair.

Table 2
Design values and ratings of the resonant network components.

	Power level /kW	Parameter	Value /μH	Nominal/Rated I /A_{rms}	Parameter	Value /nF	Nominal/Rated V /V_{rms}
GA	30	L_1	238	84/94.2	C_1	332.5	2,008/2,400
		L_{f1}	47.6	66/78.5	C_{f1}	1330	716/900
	6&11	L_1	181.4	22/31.4	C_1	25	1,670/2,000
		L_{f1}	41.2	18.2/31.4	C_{f1}	85	724/1,000
VA	30	L_2	174.3	86/94.2	C_2	500	1,368/1,600
		L_{f2}	47.6	61/78.5	C_{f2}	1330	711/900
	11	L_2	123.7	23/31.4	C_2	42.5	1,005/2,000
		L_{f2}	41.2	17.5/31.4	C_{f2}	85	724/1,000
	6	L_2	175.2	18/31.4	C_2	25	1,338/2,000
		L_{f2}	35	16/31.4	C_{f2}	100	509/1,000

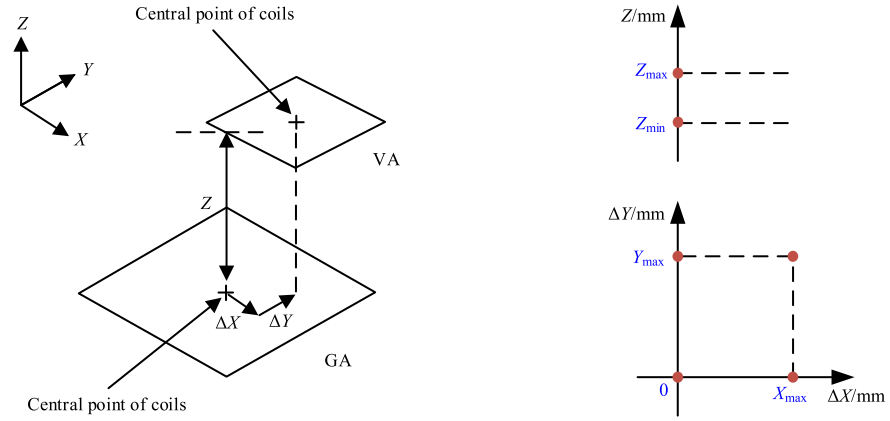

Fig. 11. Diagram of the spatial test points.

$$\boldsymbol{K} = \begin{bmatrix} 1 & 0 \\ 0 & 1 \\ 1 & 0 \\ 0 & 1 \\ 0 & 0 \end{bmatrix} \tag{9}$$

From Eq. (6), it can be seen that $\boldsymbol{L}$, $\boldsymbol{C}$, and $\boldsymbol{K}$ in the state equation are known, and the outputs $\boldsymbol{v}$ and $\boldsymbol{i}$ can be obtained by providing the input $\boldsymbol{u}$. Therefore, determining the dual-side excitation voltage values corresponding to each discrete interval in a period is crucial for solving the time-domain model. For different modulation schemes, the excitation voltage $\boldsymbol{u}$ can be represented as a matrix by traversing various possible combinations of phase shift angles. By considering the periodicity and symmetry of the waveform, the relationship between the state variables at the beginning and end of the period is derived, allowing for the calculation of the initial state variable values. Additionally, the iterative relation for discrete intervals is used to obtain the state variable values at each time step. The calculation program is written accordingly to implement the described procedure.

In addition to the above time-domain model, a circuit simulation model was developed to analyze the steady-state performance, both with and without considering cross-couplings $M_{1'f1}$ and $M_{1'f2}$. By substituting system parameters into both models, the calculated and simulated waveforms over one period are shown in Fig. 10. The results indicate that the time-domain model closely aligns with the circuit simulation model in both specific values and trend variations. The slight discrepancy between the two models can be attributed to two main factors: the inclusion of equivalent series resistances of passive elements and the non-ideal behavior of power devices in the simulation model.

As shown in Fig. 10(a), when the 30 kW coils of GA are enabled, cross-couplings induce a 17 A current in the closed loop of the 85 kHz resonant network. This obviously distorts the waveform of i_{f1} compared to a conventional LCC network, while i_{f2} remains less affected due to the relatively small value of $M_{1'f2}$. The average charging current to the battery $i_{battery}$ is increased by 1.2 A. Fig. 10(b) shows the case where the low-power GA coils are enabled, using the 6 kW VA as an example. The closed loop of 20 kHz resonant network generates a 4 A current, causing minor distortion to i_{f1} and i_{f2}, with the average charging current changing by 0.9 A. Additionally, simulation results confirm that voltage and current stress remain largely unchanged. Therefore, Eqs. (2)–(4) still provide a credible design basis. Similar performance variations were observed with the 11 kW VA.

It should be noted that the closed-loop currents impact the original current waveforms (compared to scenarios without cross-couplings) and reduce system efficiency. A potential solution is to incorporate relay switches in the closed loops, which could be toggled to prevent cross-couplings. However, this would require control signals within the GA, increasing system cost and weight, and introducing conduction loss during operation. On balance, the second integration scheme has a manageable impact on the system output performance and is ultimately adopted as the integrated solution for the GA.

After completing finite element and circuit simulations, the resulting set of parameters are finalized and summarized in Table 2. The nominal values represent the calculated voltage and current stresses under the selected parameter combination, while the ratings indicate the rated current and voltage that the chosen model can withstand. Litz wire with 1,000, 2,500, and 3,000 strands are used respectively, along with capacitors having individual values of 0.05, 0.085, 0.1, 1, and 1.33 μF. Furthermore, under the applied excitation current, the maximum magnetic flux density of the cores reaches 376 mT, which remains below the saturation thresholds of 530 mT@25 °C and 410 mT@100 °C. This validates the feasibility of utilizing a ferrite plate composed of 6.5 mm ferrite tiles.

Table 3
Mutual inductances and current at different coordinate points.

	Parameter	(0, 0, Z_{max})	(X_{max}, 0, Z_{max})	(0, Y_{max}, Z_{max})	(X_{max}, Y_{max}, Z_{max})
Main coupling/μH	M_{12}	39.5	28.4	37.3	26.9
	M_{f1f2}	5.5	4.6	3.3	2.7
Cross-couplings due to the closed-loop/μH	$M_{1'f1}$	61.8	61.7	61.5	61.4
	$M_{1'f2}$	13.4	11.9	9.2	8.1
Cross-couplings due to misalignment /μH	M_{1f2}	0	0	0	1.3
	M_{2f1}	0	0	0	1.8
	$M_{1'2}$	0	0	0	4.4
Calculated average value/A	i_{f2}	60.1	43.6	58.7	43.1
Simulated average value/A	$i_{battery}$	58.6	42.2	56.8	41.5

2.5. Misalignment analysis

Wireless charging systems are expected to maintain a certain level of output capability within the misalignment tolerance region. In this study, relevant standards are referenced, and three vertices are selected as representative positions over the tolerance region, as shown in Fig. 11. For 6- and 11-kW VAs, $X_{max} = 75$ and $Y_{max} = 100$, while for 30-kW VA, $X_{max} = Y_{max} = 100$.

Next, the 30-kW pair shown in Fig. 8(c) is analyzed as an example. The impact of misalignment on mutual inductances and outputs is investigated while keeping DC-link voltage and air gap constant at the charging mode.

Seven mutual inductance values at different spatial points are obtained through finite element simulation. Among them, M_{12}, M_{f1f2}, and $M_{1'f2}$ decrease with misalignment, while $M_{1'f1}$ remains nearly constant. M_{1f2}, M_{2f1}, and $M_{1'2}$ deviate from zero only at the coordinate point (X_{max}, Y_{max}, Z_{max}); however, their values remain small due to the presence of large air gap.

The calculated mutual inductance parameters are substituted into both the time-domain model and the circuit simulation model to obtain the average values of i_{f2} and the charging current $i_{battery}$. The summarized results are presented in Table 3.

The findings indicate that the output decreases obviously under misalignment conditions, and the output current is approximately proportional to M_{12}. In contrast, cross-couplings M_{1f2}, M_{2f1}, and $M_{1'2}$ has less influence on the output. Furthermore, simulation results suggest that DC–DC efficiency at misaligned positions is reduced by approximately 0.5–2 percentage points compared to the aligned condition. Similar analysis is also applied for other power levels, so they are not discussed in detail here.

3. System operation and control strategy

This section describes how the system operates and how it can be controlled to achieve forward and reverse power flows when interfacing multiple vehicles.

The circuit diagram of the proposed BWPT system is shown in Fig. 12. The ground-side equipment consists of a grid-side interface converter, a high-frequency (HF) FB converter, and a GA that integrates two sets of resonant networks. Each of the three vehicle-side equipment consists of a VA and a HF FB converter.

K_1 to K_4 are high-rated current relay switches with low contact resistance, toggled as needed to adapt to different vehicle-side equipment. Prior to system operation, the vehicle side equipment needs to transmit relevant information about VAs to the ground-side equipment via wireless communication. When dealing with Vehicles 1 or 2 (equipped with 6- and 11-kW VA, respectively), only K_3 and K_4 are closed, activating the 85 kHz-resonant network on the grid side. In contrast, for Vehicle 3 (equipped with a 30-kW VA), only K_1 and K_2 are switched on, enabling the 20 kHz-resonant network.

Fig. 13(a) illustrates the control block diagram of the three-phase fully-controlled rectifier. Using a dual-loop control strategy, it simultaneously regulates the DC output voltage V_0 and the gird-side AC current. Specifically, it ensures that the DC voltage remains stable while maintaining the input three-phase AC current in phase with the grid voltage, thereby improving the power factor and ensuing a total harmonic distortion (THD) of less than 5%. Fig. 13(b) shows the control diagram of

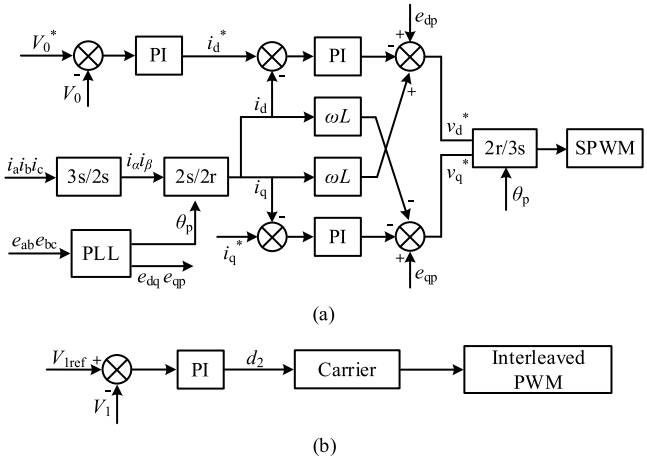

Fig. 13. Control block diagram of the front-end converter. (a) Three-phase rectifier. (b) Buck circuit.

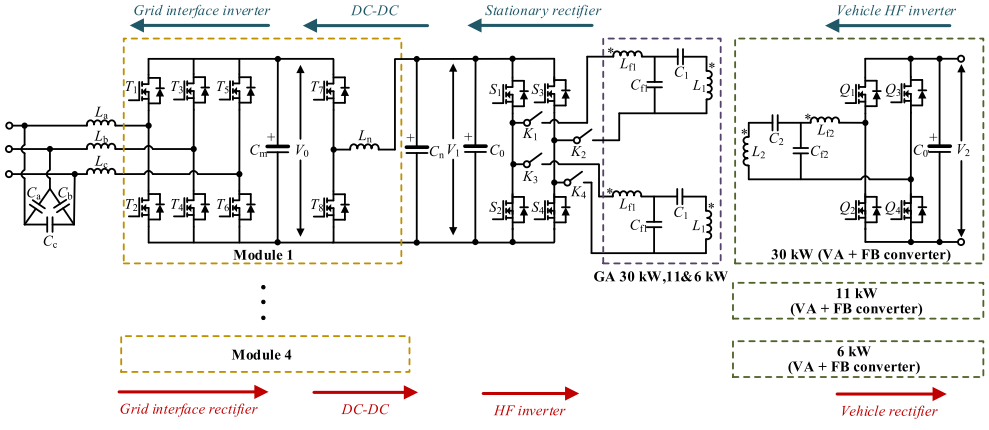

Fig. 12. System-level schematic of the proposed BWPT system.

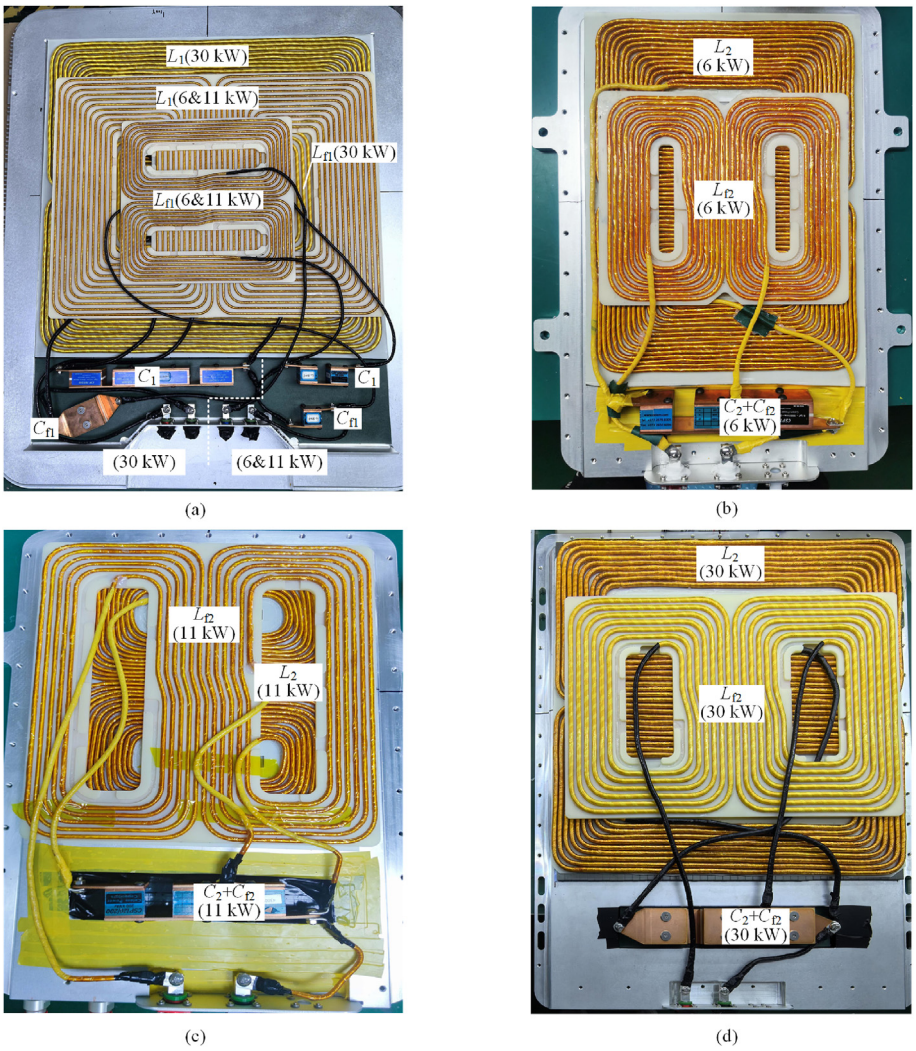

Fig. 14. (a) GA. (b) 6 kW-VA. (c) 11 kW-VA. (d) 30 kW-VA.

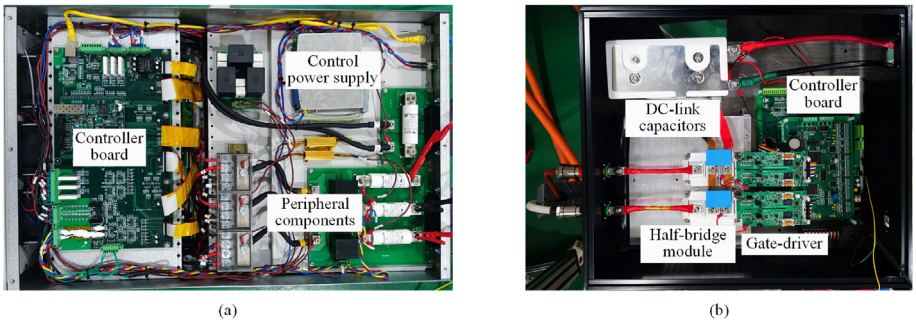

Fig. 15. (a) Grid interface converter. (b) HF inverter/rectifier.

the Buck converter, where a voltage control loop is employed to adjust the duty cycle, thereby achieving regulation of the DC voltage V_1.

For the charging mode (forward power flow or G2V mode), the FB converter on the grid side operate in inverter mode, while that on the vehicle side function in uncontrolled rectification mode. Under this condition, the output current I_{f2} is proportional to the voltage V_1, meaning the power transfer through the BIPT link is controlled by regulating V_1. Ultimately, this regulation is achieved by adjusting the duty cycle of the Buck converter stage.

For the discharging mode (reverse power flow or V2G mode), the FB converters on the vehicle side and grid side operate in inverter mode and uncontrolled rectification mode, respectively. The power flowing into the grid can similarly be controlled by adjusting the current flowing into the grid and maintaining V_1. Other alternative control methods, such as adjusting the operating frequency and phase shift angles to control the magnitude and direction of power flow [22–24], are not the focus of this work and will be explored in future studies.

4. Experimental validation

This section presents the prototypes and experimental platform of the BWPT system. The transmission performance of both grid-side and

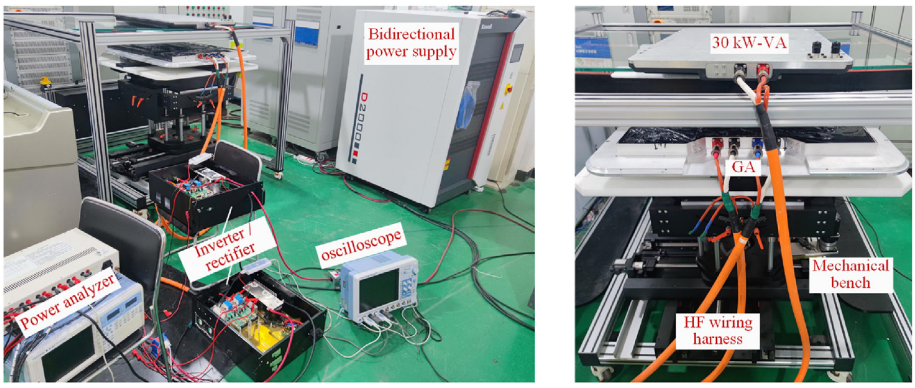

Fig. 16. The experimental setup of the BWPT system.

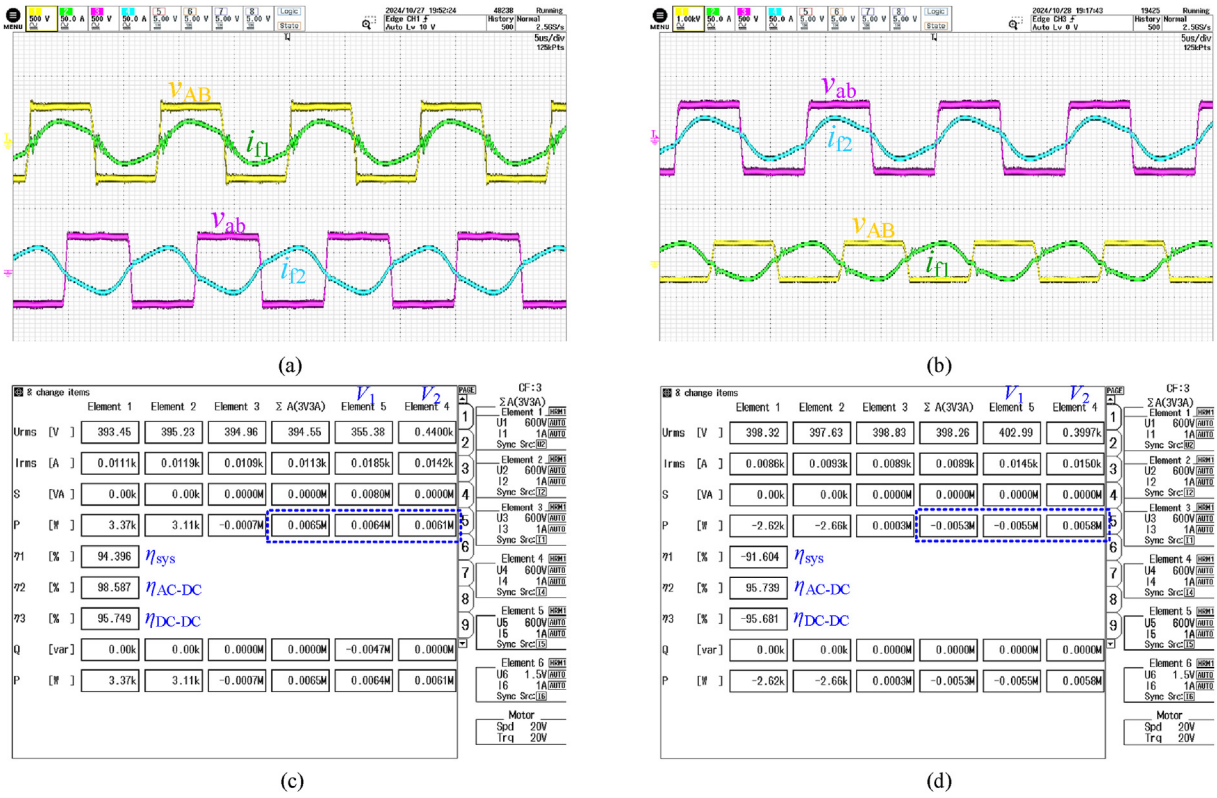

Fig. 17. Experimental voltage and current waveforms of the 6-kW prototype (a) at charging mode, (b) at discharging mode, and the corresponding results from the power analyzer, (c) at charging mode, (d) at discharging mode.

vehicle-side equipment is tested at different spatial positions under three power levels, in charging and discharging modes, and under two ground clearances.

4.1. Experimental setup

For validation purpose, the prototypes of the GA and three VAs are built, as shown in Fig. 14. It is worth noting that the measured self-inductance and mutual inductance values are closely align with the designed values, and the reliability of finite element simulation is confirmed.

Besides, the grid interface converter and HF converters are also developed, as shown in Fig. 15. The control of the front-end converter is implemented using digital signal processors (DSP) and field programmable gate array (FPGA), and a corresponding upper computer software has been developed. The HF-inverters are constructed using Wolfspeed-CAS120M12BM2 modules and AgileSwitch 62EM1 electrical drivers. Two TMS320F28335 digital signal processors function as the digital controller and pulse-width modulation generator for both the grid-side and battery-side FB converters. Signal transmission is enabled by the NRF24L01 wireless communication module.

The experimental setup of the BWPT system is shown in Fig. 16. Bidirectional DC power supply of Kewell-D2000-IV is used to simulate power batteries. DLM5058 and WT1800 are utilized as the oscilloscope and power analyzer, respectively.

4.2. Bidirectional performance test

Specifically, each prototype is tested at eight spatial points, including one aligned position and three misaligned positions across two gap

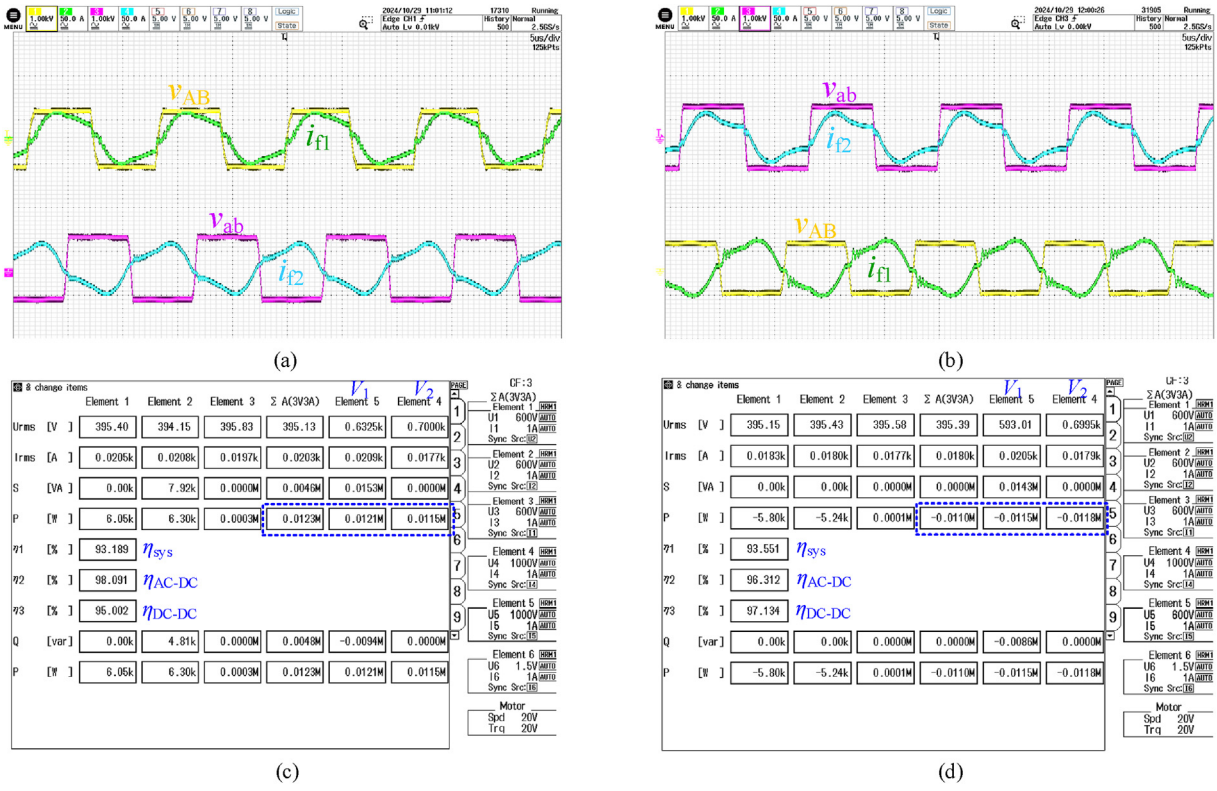

Fig. 18. Experimental voltage and current waveforms of the 11-kW prototype (a) at charging mode, (b) at discharging mode, and the corresponding results from the power analyzer, (c) at charging mode, (d) at discharging mode.

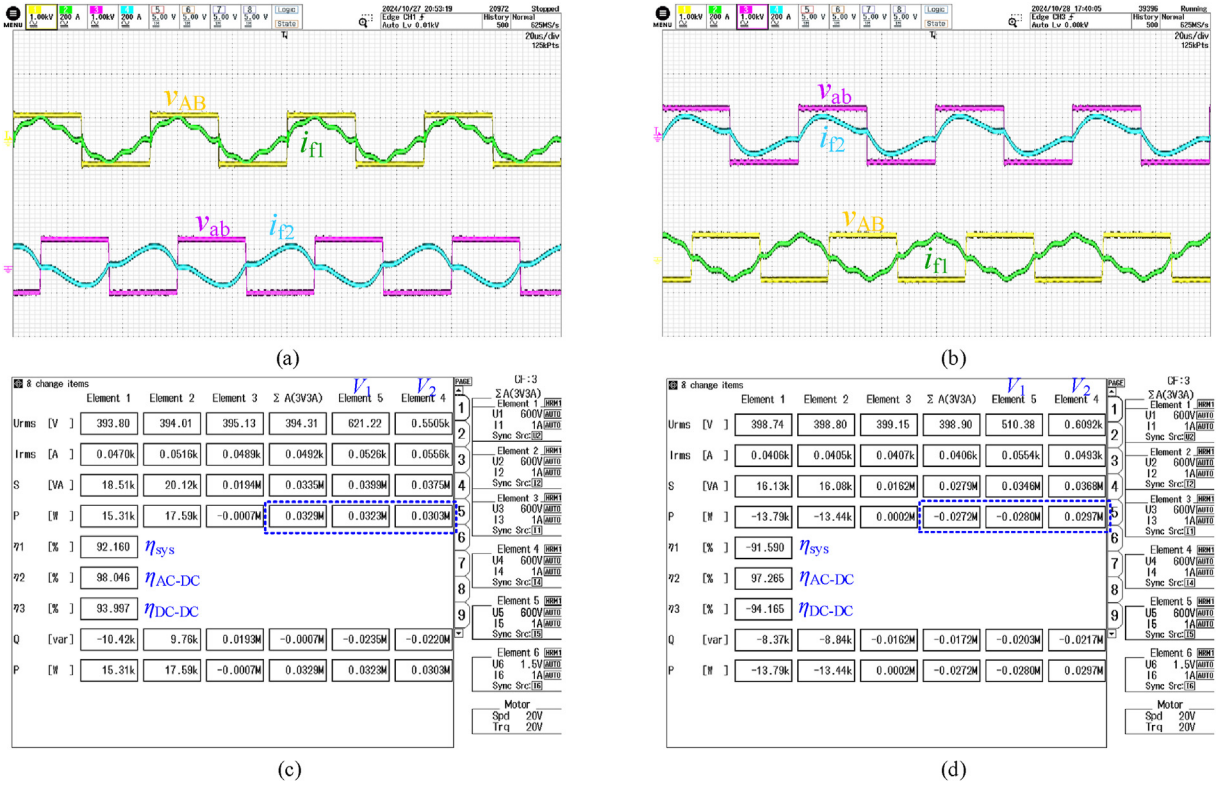

Fig. 19. Experimental voltage and current waveforms of the 30-kW prototype (a) at charging mode, (b) at discharging mode, and the corresponding results from the power analyzer, (c) at charging mode, (d) at discharging mode.

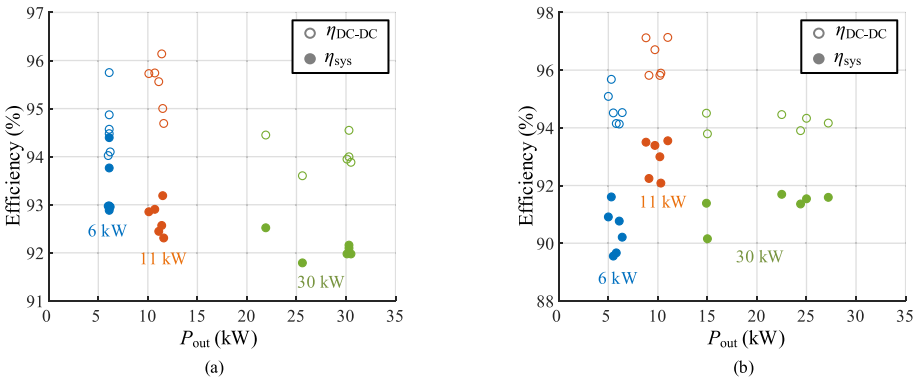

Fig. 20. Test results of the prototypes of three power levels under different voltages and ground clearances at aligned positions, (a) charging mode, (b) discharging mode.

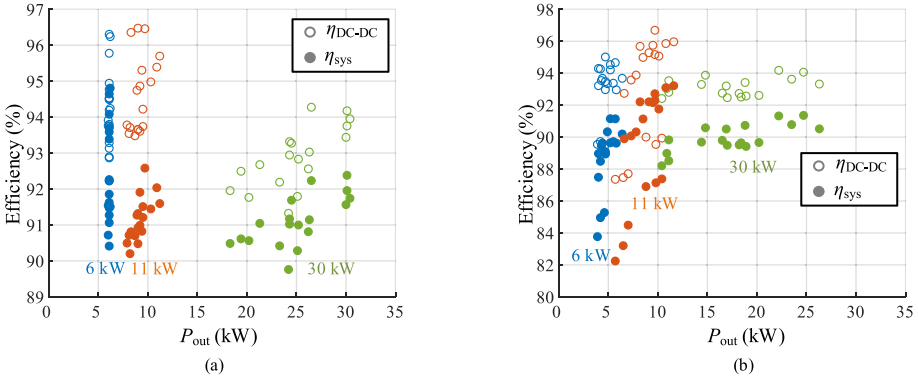

Fig. 21. Test results of the prototypes of three power levels under different voltages and ground clearances at misaligned positions, (a) charging mode, (b) discharging mode.

Table 4
Performance comparison with existing advanced BWPT systems.

Refs.	compensation topology	Power /kW	Frequency /kHz	Air gap /mm	DC-link voltage /V	Battery voltage /V	DC–DC efficiency	System efficiency
[8,25]@2014	SS	22	100	136	<800	290–410	94%–95%	91%
[2,3]@2018	TMN	7	85	140–210	360~500	280–420	92%–96%	/
[4]@2019	SS	20	85	170–250	750	300–450	94%–96%	/
[9]@2020	LCC–LCC	20	22	280	675–800	320–420	96%	93%/89%
[5]@2021	LCC-S	3.7	85	150	400	255–403	93%–94%	/
[26]@2021	LCC-S	6.6	85	140–210	390	200–420	/	92.5%
[10]@2022	SS	50	85	25	0–750	150–500	/	77%–87%
[6]@2024	S–S–S	30	/	110–150	800	610–830	91.2%–96.7%	/
Proposed@2024	Dual-coupled	30	20	185–205	200–750	420–610	93.6%–94.5%	92.5%/91.6%
	LCC–LCC	11	85	71–91		600–700	94.7%–97.1%	93.1%/93.5%
		6	85	101–121		380–440	94.0%–95.7%	94.3%/91.6%

distances. In addition, the test conditions include three voltage levels and two power flow directions, resulting in a total of 48 test points.

For the 6-kW prototype, the oscilloscope's experimental current–voltage waveforms and the respective results from the power analyzer for G2V power transfer are shown in Figs. 17 (a) and (c), respectively; and for the V2G power transfer in Figs. 17(b) and (d), η_{sys} represents the overall efficiency of the BWPT system, and $\eta_{AC\text{-}DC}$ and $\eta_{DC\text{-}DC}$ denote the efficiency of the grid interface converter and the BIPT link, respectively. Similar results for the 11- and 30-kW prototypes are presented in Figs. 18 and 19, respectively. The measured waveforms are consistent with the simulation results, which confirms the above analysis.

Under fixed DC-link voltage, battery voltage, and air gap conditions, the transmitted power and efficiency remain stable. And the power and efficiency of the prototypes under operating points at aligned position is presented as a scatter plot in Fig. 20. The experimental results confirm that the developed system supports bidirectional power flow, with the same GA capable for transferring the rated power for three VAs. Additionally, due to the meticulous design of the circuit topology and parameters, both the front-end converter and the BIPT link achieve high efficiency. Overall, the system efficiency ranges from 91.7% to 94.3% for forward transmission and from 89.5% to 93.5% for reverse transmission.

Besides, test results at misaligned positions are presented in Fig. 21. Compared to the aligned position, the output power and efficiency at the misaligned positions decrease, primarily due to the reduction in M_{12}. Increasing the bus voltage helps mitigate power reduction at misaligned positions. For example, the 6-kW pair can maintain rated power output under misalignment at charging mode. However, this approach has limitations: the grid interface converter's output voltage is constrained by an upper limit, and excessive voltage may cause passive components of the resonant networks to exceed their stress limits. Additionally, in

discharging mode, the DC-link voltage V_1 must not be too high; otherwise, low reverse voltage gain may lead to discontinuous conduction mode operation. As a result, the overall output performance in discharging mode is lower than in charging mode. In spite of this, the system efficiency of all three power–level pairs remained above 80% at the misaligned points, meeting the standard requirements for interoperability.

To emphasize advantages, a performance comparison of the proposed system and existing BWPT systems is presented in Table 4. This work demonstrates practical advancements in achieving a wide output voltage range, compatibility with multiple power levels, and efficient bidirectional energy transmission and conversion.

5. Conclusion

This work presents the design, development, and demonstrate of a high-efficiency BWPT system for multiple vehicle applications. First, a bidirectional charging and discharging system is proposed, integrating multiple power conversion stages, such as Buck and full-bridge converters, to deliver a wide output voltage range suitable for power batteries. Second, a bidirectional grid-side interface converter with modular on-demand operation is employed to achieve efficient electrical energy conversion across a broad power range. Third, a GA is designed to operate at standard-compliant frequencies and is compatible with vehicle-side equipment across various power levels. Finally, a simple yet robust control strategy is implemented to manage power flow through voltage adjustment and mode switching of the converters. This design enables the system to support multiple vehicle applications, including vehicle-side equipment ground clearance across Z1 to Z3 classes, and ensure compatibility with 400, 600, and 800 V battery platforms. Experimental results confirm interoperability between the ground-side equipment and the vehicle-side equipment. And the developed wireless bidirectional charge–discharge interface achieves a peak system efficiency of 94.3% and 93.5% in the forward and reverse power flow directions, respectively.

CRediT authorship contribution statement

Baokun Zhang: Writing – original draft, Project administration. **Junjun Deng:** Supervision, Conceptualization. **Mengchen Duan:** Methodology, Data curation. **Chang Li:** Software, Investigation. **Yi Zheng:** Validation. **Shuo Wang:** Visualization. **David Dorrell:** Writing – review & editing.

Data availability

The data and materials used to support the findings of this study are available from the corresponding author upon reasonable request.

Declaration of competing interest

The authors declare that they have no known competing financial interests or personal relationships that could have appeared to influence the work reported in this paper.

Acknowledgments

This work was supported by the National Natural Science Foundation of China under Grant 52177207 and by the Beijing Nova Program under Grant 20220484105.

References

[1] Global EV outlook 2024. https://www.iea.org/reports/global-ev-outlook-2024. [Accessed 1 December 2024].
[2] Tachikawa K, Kesler M, Atasoy O. Feasibility study of bi-directional wireless charging for vehicle-to-grid. 2018. p. 2018. https://doi.org/10.4271/2018-01-0669. 01–0669.
[3] Tachikawa K, Kesler M, Danilovic M, Esteban B, Atasoy O, Yeung K. Bi-directional wireless power transfer for vehicle-to-grid: demonstration and performance analysis. 2019. p. 2019. https://doi.org/10.4271/2019-01-0870.
[4] Sarrazin B, Derbey A, Albouy P, Ferrieux J-P, Meunier G, Schanen J-L. Bidirectional wireless power transfer system with wireless control for electrical vehicle. In: 2019 IEEE applied power electronics conference and exposition (APEC). Anaheim, CA, USA: IEEE; 2019. p. 3137–43. https://doi.org/10.1109/APEC.2019.8721800.
[5] Jou H-L, Wu J-C, Wu K-D, Kuo C-Y. Bidirectional DC-DC wireless power transfer based on LCC-C resonant compensation. IEEE Trans Power Electron 2021;36:2310–9. https://doi.org/10.1109/TPEL.2020.3005804.
[6] Mirković N, Chamorro LR, Delgado A, Alou P, Vasić M. 30 kW bidirectional inductive power transfer charger with intermediate coil for EV applications. IEEE Trans Power Electron 2024;39:9007–24. https://doi.org/10.1109/TPEL.2024.3389129.
[7] Wu S-T, Chiu Y-W. Implementation of a bidirectional 400-800V wireless EV charging system. IEEE Access 2024;12:26667–82. https://doi.org/10.1109/ACCESS.2024.3366997.
[8] Goeldi B, Tritschler J, Reichert S. Measurement results of a 22 kW bidirectional inductive charger. Nuremberg, Germany: VDE; 2015. p. 1–8.
[9] Mohammad M, Onar OC, Su G-J, Pries J, Galigekere VP, Anwar S, et al. Bidirectional LCC-LCC compensated 20 kW wireless power transfer system for medium-duty vehicle charging. IEEE Trans. Transp. Electrific. 2021;7:1205–18. https://doi.org/10.1109/TTE.2021.3049138.
[10] Gonzalez-Hernando F, Jauregi A, Villar I, Rujas A, Mir L. Z3 class 50 kW bidirectional IPT charger for EV. In: 2022 IEEE energy conversion congress and exposition (ECCE). Detroit, MI, USA: IEEE; 2022. p. 1–7. https://doi.org/10.1109/ECCE50734.2022.9947795.
[11] Song K, Lan Y, Zhang X, Jiang J, Sun C, Yang G, et al. A review on interoperability of wireless charging systems for electric vehicles. Energies 2023;16:1653. https://doi.org/10.3390/en16041653.
[12] Zhang X, Chen Z, Sha L, Yang Q, Li Y, Han D. Research on interoperability evaluation method of electric vehicle wireless charging system based on three parameter characterization. Proc CSEE 2022;42:1569–82. https://doi.org/10.13334/j.0258-8013.pcsee.201981.
[13] Lawton PAJ, Lin FJ, Covic GA, Thrimawithana DJ. A wireless synchronization controller for high-power stationary and semi-dynamic wireless charging of electric vehicles. IEEE Trans Power Electron 2023;38:13341–52. https://doi.org/10.1109/TPEL.2023.3302281.
[14] Nguyen HT, Alsawalhi JY, Hosani KA, Al-Sumaiti AS, Jaafari KAA, Byon Y-J, et al. Review map of comparative designs for wireless high-power transfer systems in EV applications: maximum efficiency, ZPA, and CC/CV modes at fixed resonance frequency independent from coupling coefficient. IEEE Trans Power Electron 2022;37:4857–76. https://doi.org/10.1109/TPEL.2021.3124293.
[15] Lu F, Zhang H, Hofmann H, Su W, Mi CC. A dual-coupled LCC-compensated IPT system with a compact magnetic coupler. IEEE Trans Power Electron 2018;33:6391–402. https://doi.org/10.1109/TPEL.2017.2748391.
[16] Ren J, Zhou K, Li H, Liu Y, Mai R. Study of dual coupled LCL topology IPT system based on DDQ coils and its anti-misalignment method. Proc CSEE 2019;39:2778–87. https://doi.org/10.13334/j.0258-8013.pcsee.172425.
[17] Deng J, Pang B, Shi W, Wang Z. A new integration method with minimized extra coupling effects using inductor and capacitor series-parallel compensation for wireless EV charger. Appl Energy 2017;207:405–16. https://doi.org/10/gcp6xz.
[18] Kan T, Nguyen T-D, White JC, Malhan RK, Mi CC. A new integration method for an electric vehicle wireless charging system using LCC compensation topology: analysis and design. IEEE Trans Power Electron 2017;32:1638–50. https://doi.org/10.1109/TPEL.2016.2552060.
[19] Kan T, Lu F, Nguyen T-D, Mercier PP, Mi CC. Integrated coil design for EV wireless charging systems using LCC compensation topology. IEEE Trans Power Electron 2018;33:9231–41. https://doi.org/10.1109/TPEL.2018.2794448.
[20] Biswas MM. Comparative study of inductive wireless power transfer pad topologies for electric vehicle charging, Master's thesis. University of Akron; 2018.
[21] Xue B, Wang L, Fu M, Wang H. State-space based universal time-domain model for voltage-fed bidirectional IPT systems. IEEE Trans Ind Electron 2024;71:615–24. https://doi.org/10.1109/TIE.2023.3247760.
[22] Zhang X, Cai T, Duan S, Feng H, Hu H, Niu J, et al. A control strategy for efficiency optimization and wide ZVS operation range in bidirectional inductive power transfer system. IEEE Trans Ind Electron 2019;66:5958–69. https://doi.org/10.1109/TIE.2018.2871794.
[23] Liu Y, Madawala UK, Mai R, He Z. An optimal multivariable control strategy for inductive power transfer systems to improve efficiency. IEEE Trans Power Electron 2020;35:8998–9010. https://doi.org/10.1109/TPEL.2020.2970780.
[24] Zhu G, Dong J, Shi W, Soeiro TB, Xu J, Bauer P. A mode-switching-based phase shift control for optimized efficiency and wide ZVS operations in wireless power transfer systems. IEEE Trans Power Electron 2023;38:5561–75. https://doi.org/10.1109/TPEL.2022.3231451.
[25] Tritschler J, Reichert S, Goeldi B. A practical investigation of a high power, bidirectional charging system for electric vehicles. In: Lappeenranta. Finland; 2014. p. 1–7. https://doi.org/10.1109/EPE.2014.6910809.
[26] Li Q. High-efficiency bidirectional inductive power transfer systems for electric vehicle charging-discharging applications, Doctoral dissertation. Huazhong University of Science and Technology; 2021.